Exploring structure–property landscape of non-fullerene acceptors for organic solar cells

View Online   Export Citation   CrossMark

Khantil Patel, Rudranarayan Khatua, (iD) **Kalyani Patrikar,** (iD) **and Anirban Mondal**[a) (iD)

AFFILIATIONS

Department of Chemistry, Indian Institute of Technology Gandhinagar, Gandhinagar, Gujarat 382355, India

[a)Author to whom correspondence should be addressed: amondal@iitgn.ac.in

ABSTRACT

We present a comprehensive analysis of the structure–property relationship in small molecule non-fullerene acceptors (NFAs) featuring an acceptor–donor–acceptor configuration employing state-of-the-art quantum chemical computational methods. Our focus lies in the strategic functionalization of halogen groups at the terminal positions of NFAs as an effective means to mitigate non-radiative voltage losses and augment photovoltaic and photophysical properties relevant to organic solar cells. Through photophysical studies, we observe a bathochromic shift in the visible region for all halogen-functionalized NFAs, except type-2, compared to the unmodified compound. Most of these functionalized compounds exhibit exciton binding energies below 0.3 eV and Δ_{LUMO} less than 0.3 eV, indicating their potential as promising candidates for organic solar cells. Selected candidate structures undergo an analysis of charge transport properties using the semi-classical Marcus theory based on hopping transport formalism. Molecular dynamics simulations followed by charge transport simulations reveal an ambipolar nature of charge transport in the investigated NFAs, with equivalent hole and electron mobilities compared to the parent compound. Our findings underscore the crucial role of end-group functionalization in enhancing the photovoltaic and photophysical characteristics of NFAs, ultimately improving the overall performance of organic solar cells. This study advances our understanding of the structure–property relationships in NFAs and provides valuable insights into the design and optimization of organic solar cell materials.

Published under an exclusive license by AIP Publishing. https://doi.org/10.1063/5.0191650

I. INTRODUCTION

In organic solar cells, pursuing high-performance materials has led researchers to delve into the intricate interplay between the molecular structure and device properties. Non-fullerene acceptors (NFAs) have emerged as promising alternatives to traditional fullerene-based acceptors,[1–4] offering advantages such as tunable energy levels, improved charge transport, and enhanced light absorption. In this context, a handful of recent studies have shown that the power conversion efficiency (PCE) of the NFAs has reached over 19%.[5–8] This transition toward NFAs underscores the significance of understanding the intricate structure–property relationships governing their behavior in organic solar cells.

A myriad of strategies have been employed within the literature to unravel the intricate structure–property relationships governing non-fullerene acceptors in organic solar cells.[9–11] Studies have focused on fine-tuning NFA structures through judicious molecular design, manipulating key parameters such as the conjugated backbone, side chain engineering, and end-group modifications.[12–15]

The conjugated backbone serves as the primary scaffold influencing electronic properties, with adjustments in the backbone length and architecture, enabling precise control over energy levels and charge transport. Concurrently, side chain engineering offers a versatile toolset for optimizing solubility, film morphology, and intermolecular interactions, crucial factors that govern the device performance.[16–18] In addition, end-group modifications are pivotal in tailoring the electron-accepting characteristics and intermolecular interactions.[19–21] Combining these strategies has helped decipher the underlying principles that dictate the correlation between the NFA structures and the resulting photophysical properties, ultimately steering the rational design of high-performance NFAs for efficient organic solar cells.

Despite the remarkable progress in understanding the structure–property relationships of NFAs for organic solar cells, the existing literature still needs to explore certain critical aspects. One notable gap lies in the comprehensive exploration of the vast chemical space available for NFA design and the systematic evaluation of the potential molecular candidates that could exhibit

12 April 2024 13:18:02

a superior performance. The sheer complexity of organic materials and the intricate interplay of numerous variables pose challenges in predicting the most optimal molecular structures through traditional experimental methods alone. This is where computational design emerges as a powerful tool to fill this void. It is possible to efficiently navigate the expansive chemical landscape by leveraging computational techniques (e.g., quantum chemistry and molecular simulations), exploring diverse molecular architectures, and predicting their electronic and optical properties.[22–25] This approach not only accelerates the materials discovery process but also allows for the identification of promising candidates with tailored properties, offering a more informed and targeted strategy for the rational design of high-performance NFAs in organic solar cells. Integrating computational design methodologies into exploring structure–property relationships can unlock novel insights and propel the field toward developing next-generation materials for efficient and sustainable energy conversion.

In this study, we investigated A–D–A′–D–A type non-fullerene acceptors—we focused on five distinct systems: BCDT-4F,[16] BCDT-4Cl,[16] PCIC-4F,[17] BTZO-4F,[18] and BFC-4F.[26] To systematically probe the structure–property relationships within these NFAs, we designed seven derivatives by strategically replacing fluorine (–F) and chlorine (–Cl) substituents with hydrogen (–H). Employing electronic structure methods and molecular dynamics simulations, we delved into the intricacies of these modified NFAs to elucidate changes in their electronic and optical properties. Our comprehensive study provides insights into the impact of subtle chemical modifications on the performance of A–D–A′–D–A type NFAs and contributes to a deeper understanding of the underlying molecular dynamics. This approach aims to unravel nuanced correlations between structural variations and device-level characteristics, paving the way for the rational design of highly efficient non-fullerene acceptors in organic solar cells.

II. COMPUTATIONAL DETAILS

A. Material selection

NFAs play a crucial role in enhancing the efficiency of organic solar cell devices by facilitating efficient charge separation and transport. Material design in this context involves tailoring the chemical structure and properties of NFAs to optimize their electronic and photophysical characteristics. Adopting suitable principles makes it possible to fine-tune the molecular architecture of NFAs, influencing factors such as energy levels, electron mobility, and absorption spectra. This customization allows for the creation of NFAs that exhibit improved performance, leading to enhanced power conversion efficiencies in organic solar cells. Small molecule acceptors (SMAs) consist of an A–D–A′–D–A type architecture, where A is the terminal acceptor moiety, D is the donor moiety, and A′ is the core acceptor moiety. Five well-known experimentally reported acceptor molecules, BTZO-4F,[18] BCDT-4F,[16] BCDT-4Cl,[16] BFC-4F,[26] and PCIC-4F,[17] were considered whose PCEs and V_{OC} values are higher than 9% and 0.75 V, respectively. Details of their photovoltaic parameters are summarized in Table S1 of the supplementary material. In addition, seven new NFAs were designed by end-group modification of the existing systems. Figure 1 illustrates the chemical structures of these compounds. The substitution of fluorine on the BTZO-4F terminal unit by hydrogen

and chlorine yielded BTZO-4H and BTZO-4Cl, whereas BCDT-4H was formed by replacing halogen groups with hydrogen in the BCDT-4F or BCDT-4Cl complex—a similar protocol generated other SMAs, such as BFC-4H, BFC-4Cl, PCIC-4H, and PCIC-4Cl. For all the investigated systems, the donor moiety consists of a cyclopentadithiophene ring with an ethylhexyl alkyl chain, whereas the terminal acceptor moiety functionalized with halogenated bis(methanylylidene)bis(3-oxo-2,3-dihydro-1H-indene-2,1-diylidene) dimalononitrile. However, the core acceptor moiety (A′) functionalized with the 2-ethylhexyl linker is different for all the four types of SMAs—benzotriazole unit for 2,2′-((2Z,2′Z)-((6,6′-(2-(2-ethylhexyl)-5,6-bis((2-ethylhexyl)oxy)-2Hbenzo[d][1,2,3]triazole-4,7-diyl)bis(4,4-bis(2-ethylhexyl)-4H-cyclopenta[1,2-:5,4-b′]dithiophene-6,2-diyl))bis(methanylylidene))bis(5,6-difluoro-3-oxo-2,3-dihydro-1Hindene-2,1-diylidene))dimalononitrile (BTZO), benzothiatriazole unit for 2,2′-((2Z,2′Z)-(((5,6-bis((2-ethylhexyl)oxy)benzo[c][1,2,5]thiadiazole-4,7-diyl)bis(4,4-bis(2-ethylhexyl)-4H-cyclopenta[2,1-b:3,4-b′]dithiophene-6,2-diyl))bis(methanylylidene))bis(5,6-difluoro]oro-3-oxo-2,3-dihydro-1H-indene-2,1-diylidene))dimalononitrile (BCDT) and 2,2′-((2Z,2′Z)-(((5,6-difluorobenzo[c][1,2,5]thiadiazole-4,7-diyl)bis(4,4-bis(2-ethylhexyl)-4H-cyclopenta[2,1-b:3,4-b′]dithiophene-6,2-diyl))bis(methanylylidene))bis(5,6-difluoro]oro-3-oxo-2,3-dihydro-1H-indene-2,1-diylidene))dimalononitrile (BFC), and benzobis(thiazole) unit for 2,2′-((2Z,2′Z)-(((2,6-dihexylbenzo[1,2-d:4,5-d′]bis(thiazole)-4,8-diyl)bis(4,4-bis(2-ethylhexyl)-4H-cyclopenta[2,1-b:3,4-b′]dithiophene-6,2-diyl))bis(methanylylidene))bis(5,6-difluoro-3-oxo-2,3-dihydro-1H-indene-2,1-diylidene))dimalononitrile (PCIC), respectively. These 12 molecules are categorized into four families, namely, BCDT-4X (type-1), BFC-4X (type-2), BTZO-4X (type-3), and PCIC-4X (type-4) (X = H, F, and Cl).

B. Electronic structure calculation

The ground state energy optimization of all investigated NFAs was performed utilizing density functional theory (DFT) implemented in the Gaussian 09 program.[27] These calculations were carried out at the ωB97XD level of theory with 6-31G(d,p) basis sets. The time-dependent density functional theory (TD-DFT)[28] was employed to perform excited state calculations, considering chloroform (CHCl₃, ε = 4.7713) as the solvent using the Polarizable Continuum Model (PCM).[29] The optimal range separation parameter (ω) for the investigated compounds was estimated by minimizing $J(ω)$ using the following equation:[30,31]

$$J(\omega) = |\text{IP}_N(\omega) + E_{N,HOMO}(\omega)| + |\text{IP}_A(\omega) + E_{A,HOMO}(\omega)|. \quad (1)$$

Here, A and N represent the anionic and neutral states, respectively. IP_N and IP_A denote the first ionization potential for the neutral and anionic states, while $E_{N,HOMO}$ and $E_{A,HOMO}$ define the HOMO energy of the neutral and anionic states, respectively. The medium dielectric constant was set to ε = 3 with the PCM solvation model, a representative value for organic materials. Therefore, the dielectric constant applied represents the solid-state medium encountered by a molecule in a thin film.[32,33] The estimated tuned ω for all the complexes is summarized in Table S3 of the supplementary material.

The optimized ω for each complex was utilized to estimate the following quantities. The energy corresponding to the S₀ to S₁ excitation (E_x) was estimated via 1240/$λ_{max}$, where TD-DFT simulations
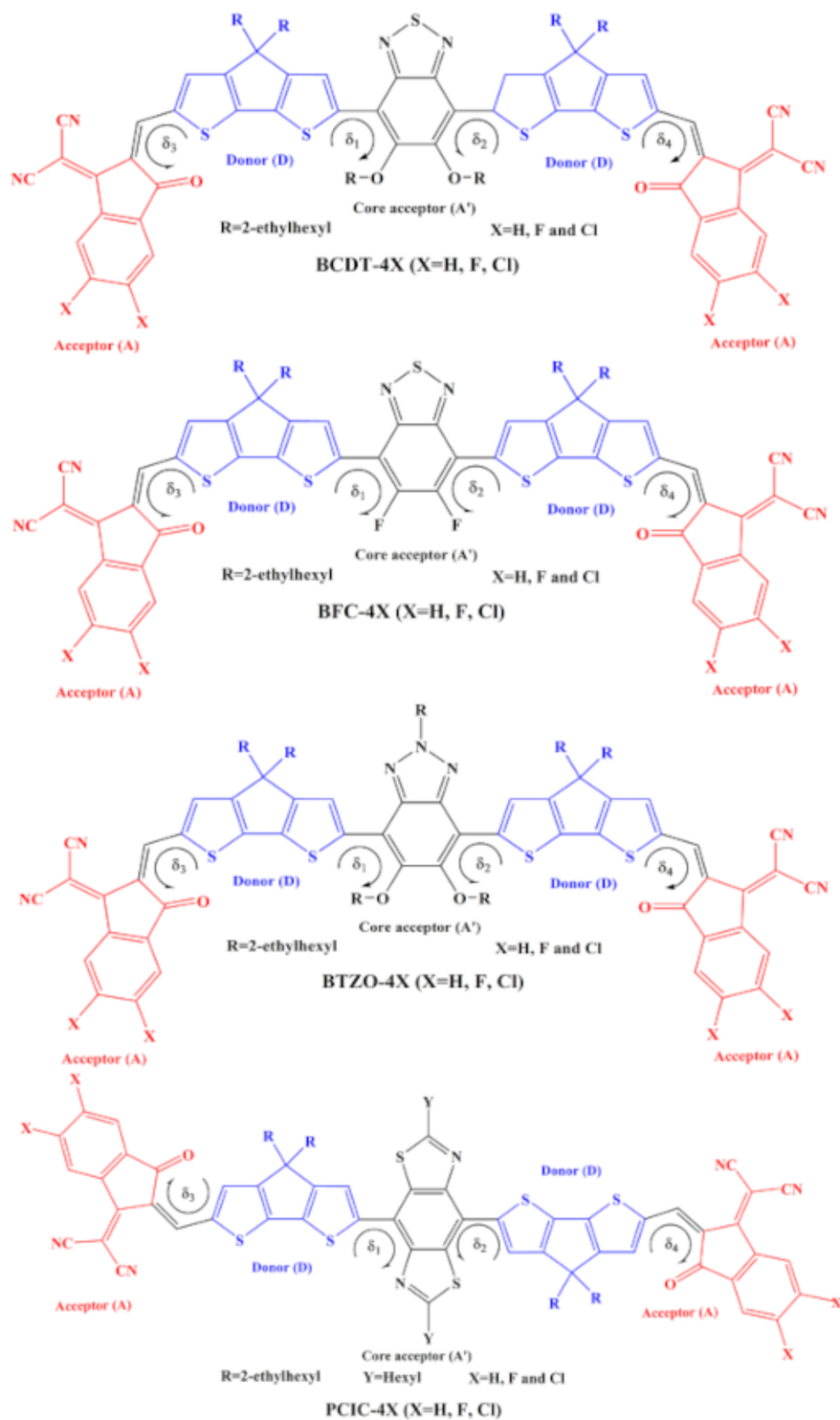
FIG. 1. Chemical structures of the investigated NFAs in the present study.

yield $\lambda_{\max}$. The exciton binding energy (E_b), the energy required to separate the coulombically bound electron and hole pair, was computed using the following equation:

$$E_b = E_{IP-EA} - E_x. \qquad (2)$$

The ionization potential (IP) and electron affinity (EA) were estimated as follows: $IP = E_c^N - E_n^N$ and $EA = E_n^N - E_a^A$, where the subscript depicts the charge state (neutral, cation, or anion) and the superscript depicts the geometry of the optimized structure. The internal reorganization energy was computed using four-point relations,[34]

$$\lambda_h = (E_n^C - E_n^N) + (E_c^N - E_c^C), \qquad (3)$$

$$\lambda_e = (E_n^A - E_n^N) + (E_a^N - E_a^A). \qquad (4)$$

Here, the subscript indicates the charge state and the superscript indicates the molecule's geometry. The open circuit voltage (V_{OC}) was evaluated using the following equation:

$$qV_{OC} = [E_{IP}^D - E_{EA}^A] - 0.3. \qquad (5)$$

Here, E_{EA}^A refers to the EA of the acceptor molecule and E_{IP}^D refers to the IP of the donor molecule. The 0.3 eV is a generally accepted value for energy loss due to energy disorder and charge recombination.[35] The PBDB-T donor molecule was chosen to perform these calculations (shown in Fig. S1 of the supplementary material). The corrected V_{OC} was estimated by subtracting an average energy difference of 1.073 V from the simulated results for each NFA. The above correction factor was computed based on the average difference between the predicted V_{OC} and experimental measurements of five NFAs, as summarized in Table S1 of the supplementary material. The quadrupole moment of all the investigated NFAs was evaluated using the Gaussian distributed multipole analysis (GDMA) program.[36]

C. Molecular dynamics simulations

Classical molecular dynamics (MD) simulations were performed on six selected NFAs using the GROMACS program suite v.2022.[37,38] These six systems include the five experimentally reported molecules and BCDT-4H. All bonded parameters were derived from the all-atom optimized potentials for liquid simulations (OPLS-AA) force field,[39,40] whereas atomic partial charges and Lennard-Jones parameters were considered using the protocol proposed by Cole *et al.*[41] Atomic partial charges were estimated from DDEC6 computation implemented in Chargemol of version 09_26_2017.[42] The σ and ε parameters in the Lennard-Jones potential were derived using the Tkatchenko–Scheffler (TS) scheme,[43] where the radius of the free atom in vacuum was taken from Ref. 41. The initial configuration of the materials was generated by randomly placing 1000 molecules in a cubic box of dimensions $250 \times 250 \times 250$ Å^3 using the Packmol package.[44] The above initial structures were energy-minimized and annealed from 300 to 800 K within 5 ns, followed by rapid quenching to 300 K within 3 ns. Further equilibration for 5 ns was performed at 300 K. All simulations were performed in the *NPT* ensemble using a canonical velocity rescaling thermostat,[45]

a Berendsen barostat for pressure coupling,[46] and the smooth particle mesh Ewald technique for long-range electrostatic interactions. A time step of 0.5 fs was used to integrate the equations of motion. Non-bonded interactions were computed with a real-space cutoff of 1.3 nm.

D. Charge transport calculation

The simulated morphology was taken to extract all possible dimers with an intermolecular distance less than 10 Å to investigate charge transport characteristics further. A maximum of 100 dimers were selected for the above analysis. The charge transfer integral in a dimer was estimated using the ChArge TraNsfer Integral Package (CATNIP) program[47] by considering the output generated from the Gaussian 09 calculations at the B3LYP/6-31G(d,p) [IOP(3/33 = 1)] level of theory. The charge transport rate of the investigated system was evaluated using the semi-classical Marcus theory based on the hopping transport formalism,[48,49]

$$k_{12} = J_{12}^2 \sqrt{\frac{\pi}{\hbar^2 k_B T\lambda}} \exp\left[-\frac{(\Delta E_{12} - \lambda)^2}{4k_B T\lambda}\right]. \qquad (6)$$

Here, $\Delta E_{12} = \sqrt{(\varepsilon_1 - \varepsilon_2)^2 - 4H_{12}^2}$, where ε_1 and ε_2 are the effective site energies of the dimer; k_B is the Boltzmann constant; λ is the internal reorganization energy; and T is the temperature (298 K). The Marcus equation is considered to be suitable for calculating the rates of these systems, as the reorganization energy of the molecules is high and hence dominates the electron–phonon coupling effects.[50] The following relation was used to evaluate the effective site energies of the fragments of a dimer:

$$\varepsilon_{1(2)} = \frac{(e_1 + e_2) - H_{12}S_{12} + (e_1 - e_2)\sqrt{1 - S_{12}^2}}{2(1 - S_{12}^2)}. \qquad (7)$$

The electronic coupling elements (J_{12}) were estimated using the following equation:

$$J_{12} = \frac{H_{12} - S_{12}(e_1 + e_2)/2}{1 - S_{12}^2}. \qquad (8)$$

Here, e_1 and e_2 are the site energies of the monomers in a dimer, S_{12} is the spatial overlap matrix element, and H_{12} is the transfer integral of the dimer in the molecular system. The charge carrier mobility of the NFAs was estimated from the diffusion process, in which the charge carriers hop from one site of the molecular fragments in a dimer to another. Charge carrier mobility was calculated by implementing a kinetic Monte Carlo (kMC) algorithm using an in-house code run in Python. A grid of $400 \times 400 \times 400$ sites was set up with the intersite distance based on the radial distribution functions obtained from MD simulated morphologies. A sequence of electron or hole hops was simulated with the rate of charge transfer between pairs of sites having values randomly drawn from those calculated by the Marcus equation for different configurations. The mobility was calculated as an average of 10 000 trials, each run for 100 ns.

III. RESULTS AND DISCUSSION

A. Molecular geometry

The chemical structures of the investigated NFAs are illustrated in Fig. 1. In all NFAs, the core acceptor unit is fused with the donor via a single covalent bond. In contrast, the terminal acceptor unit is attached to the donor via a vinyl linker. The topology of the type-1, type-2, type-3, and type-4 systems is analyzed based on their connections between donor fragments and core and terminal acceptor moieties. The computed dihedral angles and ground-state dipole moments of all NFAs are summarized in Table S2 of the supplementary material. As seen from Table S2 of the supplementary material, core acceptor moieties benzothiatriazole and benzobisthiazole of type-1 and type-4 are highly twisted from the donor units with maximum torsional angles of $67.84°(\delta_1)$ and $62.26°(\delta_2)$ as compared to type-2 $(36.13°)$ and type-3 $(57.05°)$ NFAs. The above geometry changes are significant due to the presence of the longer alkyl chain and the increase in the π-conjugation length of the core acceptor unit in the molecular system. However, a minimal torsional angle (δ_3 and δ_4) is observed in the acceptor–donor connection, which makes the molecule planar at the end position of the system. As seen from Table S2 of the supplementary material, type-1 NFAs possess the highest ground-state dipole moments among the investigated systems, whereas the lowest dipole moment was observed in the case of type-4 NFAs. Type-2 and type-3 NFAs exhibit dipole moments in the intermediate range. Generally, a high dipole moment enables improved charge separation and easy film fabrication through enhanced solubility in organic solvents.[51]

B. Electrostatic potential maps

Electrostatic potential (ESP) maps in NFAs play a pivotal role in shaping the electronic landscape within these organic molecules, subsequently influencing the current density and PCE in organic photovoltaic devices. In regions with higher electrostatic potential, electrons are more likely to accumulate, fostering efficient charge separation and facilitating the formation of a charge-transfer complex. This localized charge distribution affects the current density by influencing the rate of charge carrier transport through the NFA material. Moreover, the potential gradients between the donor and acceptor units dictate the driving force for charge separation and, consequently, impact the open-circuit voltage of the solar cell. The electrostatic potential maps provide insights into the surface charge distribution within the molecule, resulting in positive, negative, and neutral charge regions. Figure 2 directly compares the distribution for the NFAs, whereas the bare and chlorinated NFAs are shown in Fig. S2 of the supplementary material. For all four types of NFAs, the regions with positive ESP, represented by the mint color, appear in the central core of the π-conjugated system. In contrast, the negative ESP is observed at the –CN and –O groups attached to the end-group acceptor. As evident from Figs. 2 and S2 of the supplementary material, it is observed that the halogen atoms attached at the terminal unit influence the ESP value by increasing the electronic cloud in the terminal units, which is highly desired to tune the electronic and photovoltaic characteristics of the organic solar cells (OSCs). As reported in Ref. 52, introducing an electron-rich unit at the terminal negatively impacts electrostatic potential values, decreasing the current density and PCEs. Meanwhile, adding an electron-deficient unit contributes to enhancing the ESP values. They noticed that
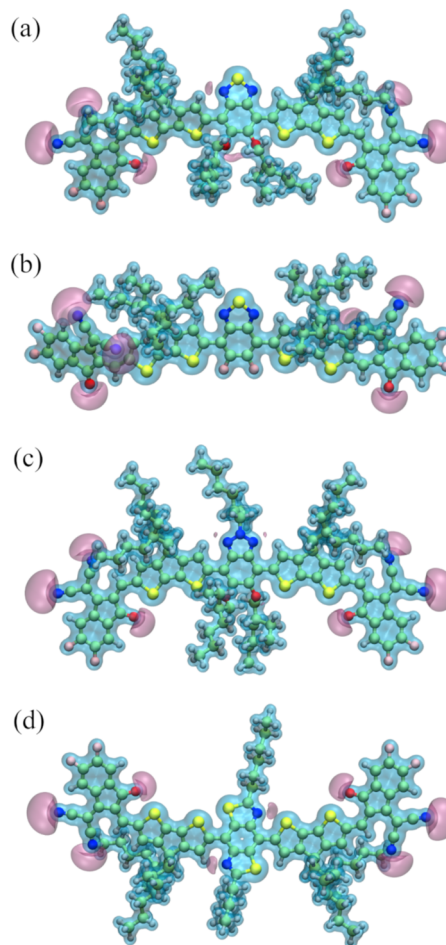

FIG. 2. Iso-electrostatic potential surfaces of selected non-fullerene acceptors: (a) BCDT-4F, (b) BFC-4F, (c) BTZO-4F, and (d) PCIC-4F. Similar surface plots for the remaining systems are shown in Fig. S2 of the supplementary material.

introducing chlorine atoms increased the dielectric constant, subsequently decreasing the exciton binding energy. Based on our ESP analysis, we exhibited a notable overall increase in electron density within the halogenated NFAs compared to their respective parent molecules.

C. Molecular orbitals

Molecular orbital positions and distributions are compared for all NFAs in Fig. 3, whereas others are provided in Fig. S3 of the supplementary material. The cyan (pink) colored molecular orbitals represent the HOMO (LUMO) of the investigated systems. Figure 3 shows that both HOMO and LUMO are evenly distributed onto the donor moiety linking with the core acceptor units of the molecular system. However, end-capped acceptor moieties contribute significantly to the LUMO, making the overall molecule act as an acceptor. The nitrogen–sulfur–nitrogen (N–S–N) containing core in the type-1 and type-2 NFAs contributed significantly to the LUMO compared to the type-3 and type-4 systems. Meanwhile, the nitrogen–nitrogen–nitrogen (N–N–N) and sulfur–carbon–nitrogen
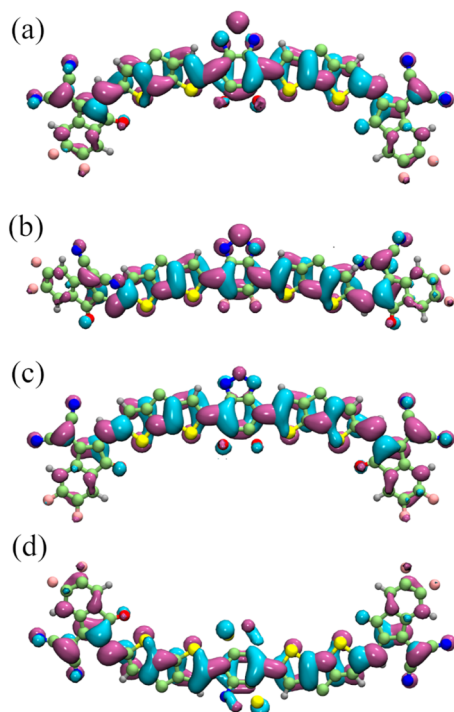
12 April 2024 13:18:02

FIG. 3. Frontier molecular orbitals (HOMO and LUMO) in selected non-fullerene acceptors: (a) BCDT-4F, (b) BFC-4F, (c) BTZO-4F, and (d) PCIC-4F. Similar surface plots for the remaining systems are shown in Fig. S3 of the supplementary material.

(S–C–N) containing the core units of type-3 and type-4 NFAs exhibit a higher contribution to HOMO than LUMO, as shown in Figs. 3 and S3 of supplementary material. As can be seen from Figs. 3 and S3 of the supplementary material, in the type-1 systems, the electron distribution of the LUMO is slightly shifted toward the terminal acceptor moieties fused with the halogen group rather than the parent molecule attributed to the presence of electron-withdrawing halogen groups. Moreover, the HOMO–LUMO (H–L) gap is significantly affected by the halogen-functionalized NFAs. As summarized in Table S2, except for type-2 compounds, the H–L gap decreases as a decrease in the electron negativity from –F to –Cl. Moreover, N–S–N and N–N–N containing type-2 and type-3 NFAs showed a slight decrease in the HOMO–LUMO gap than the type-1 and type-4 NFAs, which is possible due to the enhancement of the LUMO character in the former than the latter.

D. Energy levels

Ionization potential and electron affinity are essential parameters for controlling the charge transport properties of non-fullerene acceptors. Reference 53 notes that trap-free electron and hole transport in organic semiconductors are observed when EA and IP values are within the 3.4–6.0 eV window. The IP and EA of the investigated NFAs are summarized in Table S3 of the supplementary material. As evident, the gas-phase energy levels in these examined NFAs are very close or within this window, showcasing their probability of exhibiting excellent charge carrier transport. The introduction of halogen atoms leads to an increase in the electron

affinity of the NFA. The addition of halogen atoms enhances the electron-attracting nature of the molecule, effectively increasing the electron affinity and making it easier for the NFA to accept an electron during the photoexcitation and charge separation process in a photovoltaic device.

Reorganization energy (λ) is a critical parameter determining the charge transport characteristics in organic materials. Generally, carrier mobility exhibits an inverse correlation with the reorganization energies, i.e., lower λ corresponds to faster charge transport. The reorganization energy values of the NFAs are summarized in Table S3 of the supplementary material. As can be seen from Table S3 of the supplementary material, the λ_e values of all NFAs, except BFC-4X, are found to be smaller than the hole. Such a larger λ_h of BCDT-4X, BTZO-4X, and PCIC-4X can be elucidated based on the twisted molecular geometry arising from larger dihedral angles at the end-capped acceptor units. In the case of BFC-4X compounds, λ_h (0.23–0.33 eV) and λ_e (0.25–0.33 eV) are found to be similar. In type-1, type-3, and type-4 complexes, the net decrease in λ_e is estimated around 0.11–0.29 eV, than the hole. Thus, it indicates that the significantly lower λ_e than that of λ_h possesses better electron transport characteristics than the hole.
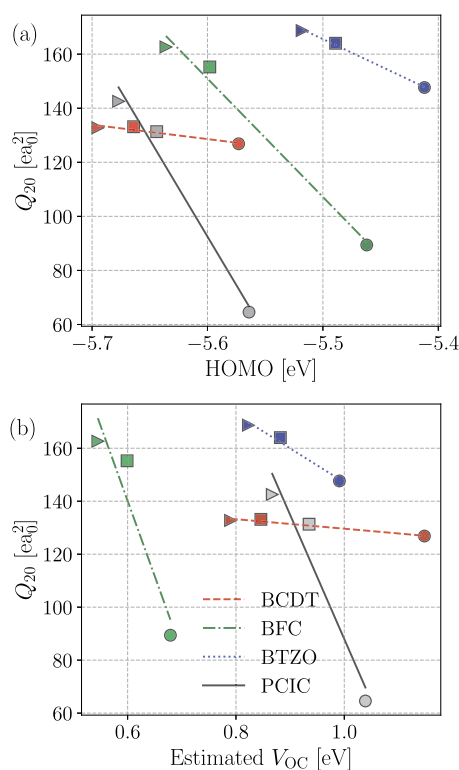

FIG. 4. (a) Q_{20} against HOMO levels, the color of each point represents the corresponding $\Delta_{HOMO-LUMO}$ gap, and (b) Q_{20} against V_{OC}, the color of the point represents the corresponding Δ_{LUMO} gap. The presence of hydrogen, fluorine, and chlorine in the terminal positions is represented by circle, square, and triangle, respectively.

E. Quadrupole moment

In NFAs, where efficient charge separation and transport are critical for photovoltaic performance, the orientation of the molecular dipoles is essential. The quadrupole moment perpendicular to the π-system (Q_{20}) influences the molecular alignment and interactions within the active layer of an organic solar cell. An optimal quadrupole moment perpendicular to the π-system can lead to the ideal orientation of NFAs, promoting favorable charge transfer pathways and reducing recombination losses. In addition, Q_{20} contributes to the organization of NFAs in the active layer, affecting the packing and intermolecular interactions. An optimal value of Q_{20} helps achieve a desirable molecular arrangement that facilitates efficient exciton dissociation and charge carrier mobility.[20] Q_{20} regulates the photovoltaic parameters such as short-circuit current (J_{SC}) and power conversion efficiency (PCE) of the organic solar cell. A higher value of Q_{20} generally enhances the J_{SC}, whereas V_{OC} is significantly affected negatively.[11,20,54] Thus, a balanced J_{SC} and V_{OC} are highly required for achieving efficient OSCs. The computed quadrupole moment perpendicular to the π-system for all the investigated NFAs is summarized in Table S4 of the supplementary material. Figure 4(a) displays the correlation between Q_{20} and the HOMO energy, while the color of each point depicts the magnitude of the $\Delta_{HOMO-LUMO}$ gap. As can be seen, halogen incorporation yields an increased Q_{20} with a deeper HOMO energy level. The quadrupole moment, which characterizes the charge distribution within the NFA molecules, correlates with the spatial arrangement of electron density. This distribution, in turn, affects the HOMO energy. A higher quadrupole moment is generally associated with a more dispersed charge, potentially leading to a shift in the HOMO energy. In addition, the $\Delta_{HOMO-LUMO}$ gap is influenced by the quadrupole moment. Changes in charge distribution and spatial orientation impact the energy levels of molecular orbitals, affecting the energy required for charge transfer processes. Precisely, alterations in the quadrupole moment can modulate the $\Delta_{HOMO-LUMO}$ gap, influencing the absorption spectrum and the ability of NFAs to absorb photons and generate charge carriers. Modulating the quadrupole moment through molecular design not only alters the charge distribution within the molecules but also influences the electronic structure, impacting the HOMO energy and the $\Delta_{HOMO-LUMO}$ gap. This intricate interplay is critical for optimizing the photophys-

ical properties of NFAs in organic solar cells, ultimately enhancing their efficiency and performance.

Figure 4(b) shows the correlation between V_{OC} and Q_{20}, where the points are colored based on the magnitude of the difference between LUMO and LUMO+1, termed as Δ_{LUMO}. V_{OC} of the investigated NFAs was estimated by considering the PBDB-T donor, as shown in Fig. S1 of the supplementary material, and the obtained results are summarized in Table S4 of the supplementary material. As seen from Fig. 4(b), the inverse correlation between Q_{20} and V_{OC} is observed in all NFAs, which is in accordance with earlier studies as cited in Refs. 11, 20, and 54. The estimated V_{OC} values lie in the range of 0.55–1.15 V with a general trend of decreasing V_{OC} upon halogenation. Moreover, the computed Δ_{LUMO} values are consistently found to be lower than 0.35 eV (Table S3 of the supplementary material). The smaller Δ_{LUMO}, along with a sufficiently low-lying LUMO+1 level in the acceptor, enhances the probability of accepting electrons from the donor's LUMO.[55,56] Furthermore, the smaller Δ_{LUMO} is required to enable the high energy charge transfer (CT) state, significantly enhancing the charge separation process, which, in turn, leads to a notable enhancement in power conversion efficiency. In type-1 complexes, the Δ_{LUMO} decreases from H to F to Cl and follows a similar trend for the remaining complexes. In Fig. 4(b), it is evident that most of the complexes display reduced Δ_{LUMO}, corresponding to a higher open-circuit voltage exceeding 0.8 V. Hence, Δ_{LUMO} acts as a crucial parameter to determine the efficiency of NFAs for high-performance OSCs.

F. Photophysical properties

The photophysical properties of the NFAs are analyzed at the TD-DFT/ωB97XD/6-31G(d,p) level using CHCl$_3$ as the solvent. The examined photophysical parameters, such as maximum absorption wavelength (λ_{max}), excitation energy (E_x), oscillator strength (f), and exciton binding energy (E_b), of the NFAs are summarized in Table S4 of the supplementary material. It is evident that all halogenated NFAs, except type-2, possess a bathochromic shift from H to F to Cl compared to their parent compound. The above shifting is due to the electron-withdrawing group (i.e., –F and –Cl) functionalized at the end-group acceptor moieties of the NFAs. The maximum shifting ~20 nm is observed in halogenated type-3 NFAs compared to the parent molecule. The estimated λ_{max} of investigated NFA lies
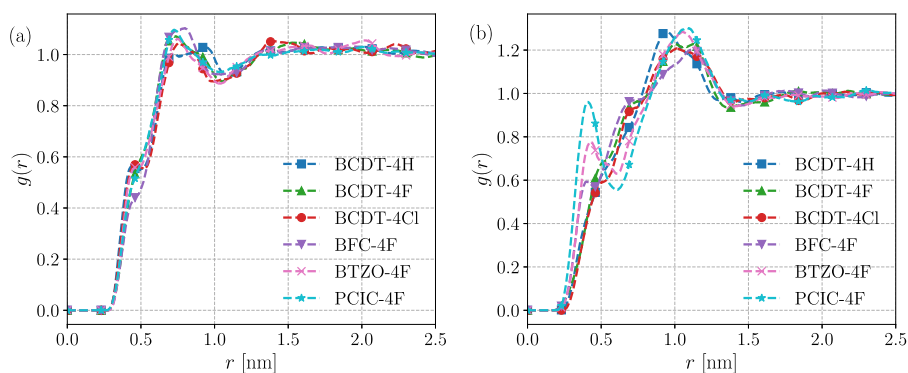

FIG. 5. Radial distribution function (RDF) between (a) terminal–terminal (T–T) and (b) core–terminal (C–T) moieties in the selected complexes computed from MD simulation trajectories.

in the visible regions of wavelength ~597–746 nm. Table S4 of the supplementary material shows that N–S–N containing type-2 NFAs possess maximum wavelength corresponding to the electronic excitation from S_0 to S_1, mainly associated with the electronic transition from HOMO → LUMO. A similar nature of the significant electronic transitions (HOMO → LUMO) occurs for the remaining systems. The computed oscillator strengths fall in the range of 2.19–3.06, indicating strong light absorption abilities in these NFAs.

Exciton binding energy is one of the crucial parameters governing an organic solar cell's overall efficiency and performance. The exciton binding energy of the NFAs was estimated using Eq. (2). The computed E_b values of the complexes are summarized in Table S4 of the supplementary material. As anticipated, a low exciton binding energy is preferred for spontaneous free charge carrier generation, leading to enhanced J_{SC}. It is evident from Table S4 of the supplementary material that the E_b values of the halogen functionalized NFAs are reduced significantly in comparison with their bare system. However, no such significant changes are noted for type-3 NFA systems. It is evident from Fig. 1 that the type-3 complexes possess more units of an alkyl linker, which may significantly change the geometry and impact E_b.

G. Charge transport simulations

To understand the effects of structural variations along the core acceptor units on the charge transport efficiencies of the studied NFAs, we performed molecular dynamics simulations on selected NFAs and generated their amorphous morphology. Due to the increased computational cost associated with charge transport simulations, six systems were considered: type-1 NFAs, fluorinated type-2, type-3, and type-4 NFAs. The above simulations were carried out by considering 1000 acceptor molecules packed into a cubic box, followed by simulated annealing and rapid quenching to obtain their amorphous morphology. For example, Fig. S4 of the supplementary material displays the amorphous morphology of the BTZO-4F compound. These morphologies were then used to compute the radial distribution functions (RDFs) between terminals-to-terminals (T–T) and core-to-terminal (C–T) units. The computed RDFs are illustrated in Fig. 5. The RDFs show a more continuous and broad distribution of distances for an amorphous

material, indicating the absence of long-range order. The lack of sharp peaks in the RDF reflects the randomness in the arrangement of atoms, with short-range order still present but without any periodicity. As shown in Fig. 5, the RDFs of the T–T units showed a significant peak near 9 Å, whereas the C–T units are observed at 10 Å. The prominent peaks at T–T and C–T of all NFAs are broader, indicating an amorphous type of packing arrangement.

We have extracted around 100 molecular dimers from the simulated morphology by setting the centroid-to-centroid distance criteria of <10 Å. The charge transport parameters, electronic coupling, charge transport rate, and mobility were computed on 100 dimers using Eq. (6). The site energy differences (ΔE_{12})
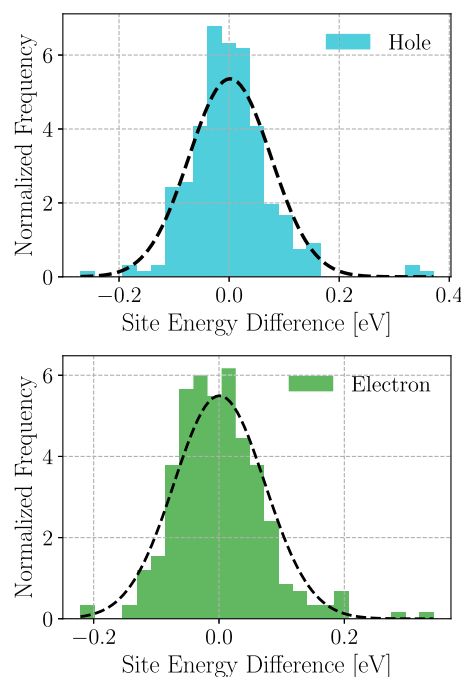
FIG. 6. Distribution of site energy differences for hole and electron transfer process in the selected NFA systems.
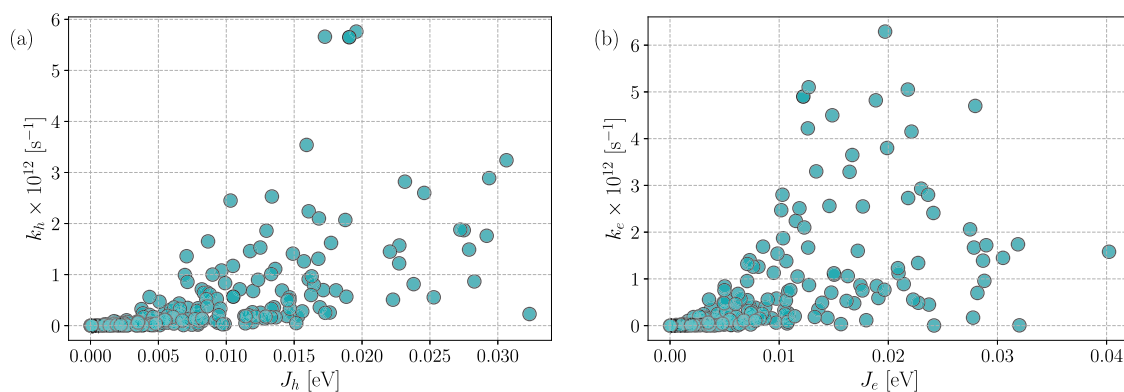
FIG. 7. Correlation plots between the charge transport rates (k_h and k_e) and electronic coupling (J_h and J_e) for (a) holes and (b) electrons of the selected NFAs.

TABLE I. Computed rates of hole and electron transfer (k_h and k_e) in s^{-1} and their mobility (μ_h and μ_e) in cm^2 V^{-1} s^{-1} of the six selected NFAs. The experimental hole and electron mobilities (μ_h^{exp} and μ_e^{exp}) are included wherever available.

Compounds	k_h	k_e	μ_h	μ_e	μ_h^{exp}	μ_e^{exp}
BCDT-4H	1.25×10^{11}	1.88×10^{11}	3.322×10^{-5}	4.270×10^{-5}	⋯	⋯
BCDT-4F[16]	4.15×10^{10}	1.18×10^{11}	1.921×10^{-5}	3.471×10^{-5}	2.60×10^{-4}	2.09×10^{-4}
BCDT-4Cl[16]	1.12×10^{11}	2.63×10^{11}	2.726×10^{-5}	4.956×10^{-5}	3.73×10^{-4}	3.54×10^{-4}
BFC-4F[26]	1.96×10^{11}	1.05×10^{11}	4.193×10^{-5}	3.249×10^{-5}	1.78×10^{-4}	5.91×10^{-5}
BTZO-4F[18]	3.51×10^{10}	4.0×10^{11}	1.933×10^{-5}	6.046×10^{-5}	3.47×10^{-4}	3.26×10^{-4}
PCIC-4F[17]	2.52×10^{10}	5.36×10^{11}	1.671×10^{-5}	6.252×10^{-5}	2.63×10^{-4}	1.84×10^{-4}

between the fragments of each dimer for hole and electron are illustrated in Fig. 6. As depicted in Fig. 6, ΔE_{12} for holes and electrons follows a Gaussian distribution with width 0.14 and 0.16 eV, respectively, similar to the earlier report based on 2,2′-((2Z,2′Z)-((4,4,9,9-tetrahexyl-4,9-dihydro-s-indaceno [1,2-b:5,6-b′]dithiophene-2,7-diyl)bis(methanylylidene))bis(3-oxo-2,3-dihydro-1H-indene-2,1-diylidene))dimalononitrile (IDIC) NFAs.[57] The energy disorder is quantified by ΔE_{12}, and the expected disorder for hole and electron transfer in the studied systems is of the same order as that reported in Ref. 57 for amorphous NFAs.

Electronic coupling (J_{12}) is an essential parameter governing the charge carrier transport rate and mobility. Its value depends on the molecular overlaps between the dimer fragments, and thus, the orientational and packing between molecular dimers play an important role here. Generally, a higher magnitude of J_{12} yields a larger rate of charge carrier transport (k_{12}) and mobility (μ). Notably, high values of reorganization energy may negatively impact the rate of charge transport, as seen in Eq. (6). Thus, a lower reorganization energy is always preferred to achieve larger hole and electron mobility. The correlation between the electronic coupling elements and the rate of charge transfer for holes and electrons in the six selected NFA systems is illustrated in Fig. 7. It is important to note that these results are obtained from calculations performed on 100 molecular dimers selected for each compound from MD simulation trajectories. In Fig. 7, it is observed that the coupling elements (J_h and J_e) of a maximum number of dimers lie below 0.01 eV. Nevertheless, significant pairs possess coupling element values greater than 0.01 eV. Even for a few dimers, the electronic coupling is higher than 0.03 eV, implying a large constructive overlap between frontier orbitals, HOMO and LUMO, between the molecular fragments of the dimer separated at a smaller intermolecular distance. These few pairs are anticipated to exhibit better charge transport rates and mobility.

Table I summarizes the computed hole and electron mobilities (μ_h and μ_e) calculated based on the kMC method for the investigated systems, and they are compared against the experimental measurements wherever available. The computed mobilities are found to be in close agreement with the experimental values for all cases. As seen from Table I, hole and electron mobilities in these complexes are almost the same order of magnitudes, showcasing the ambipolar nature of charge transport. Such ambipolar charge transport characteristics were also anticipated based on the gas-phase ionization energy and electron affinity values, which were found to be located within the trap-free window as given in Table S3 of

the supplementary material.[53] Charge separation and recombination effects with donor polymers or morphology of donor–acceptor interface have not been included, as these require a large-scale study.

IV. CONCLUSIONS

In summary, we explored the structure–property relationship among four different types of halogen-functionalized NFAs via multiscale simulations. Seven out of 12 NFAs are designed based on the end-group modification in the terminal acceptor unit of the A–D–A′–D–A architecture. The materials selection was focused on the functionalization of halogen atoms (i.e., –F and –Cl) at the terminal position and the incorporation of varying core acceptor units within the NFA structure. Structural optimization and electronic properties were determined within the density functional theory framework, considering ground and excited-state formalism. These calculations were performed using range-separated functional ωB97XD, where the optimum ω for each NFA was optimized before the final computation was done.

The results obtained from the above quantum chemical calculations helped us understand the geometrical, electronic, and photovoltaic characteristics of the halogen-functionalized NFAs. The geometrical analysis carried out by estimating dihedral angles at the junction of donor and acceptor units revealed that type-2 and type-3 complexes exhibit a smaller dihedral angle value, indicating a more planar geometry when compared to the other complexes. In type-1 and type-4 complexes, the larger dihedral angle is observed due to the longer alkyl chain and the increase in the π-conjugation length of the core acceptor unit in the molecular system. These systems exhibited a nonplanar geometry with a maximum twisting angle of 67.84°. Altering the electron-withdrawing halogen group in the terminal acceptor unit of non-fullerene acceptors substantially influenced the energy levels, electron affinity, ionization potential, and reorganization energy values. The $\Delta_{HOMO–LUMO}$ gap decreases as a decrease in the electronegativity from –F to –Cl, whereas EA increases as compared to the parent compounds. The increased EA values in halogen-functionalized acceptors imply improved electron transport characteristics. All the investigated systems exhibited absorption in the UV–visible region with halogen incorporation, leading to a bathochromic shift compared to bare systems. Except for a few complexes BCDT-4H, BFC-4H, and PCIC-4H, all other systems exhibited Δ_{LUMO} and E_b lower than 0.3 eV, implying a higher propensity to form a high energy CT state and thus leading to

the spontaneous formation of charge separated state and hence free charge carrier generation.

The charge transport simulations were performed for the six selected NFAs. Amorphous morphologies generated via molecular dynamics simulations were used to further compute hole and electron mobilities. Although the predicted charge carrier mobility underestimated the reported experimental measurements, the trend observed in both approaches is the same. Most complexes possess balanced ambipolar transport of both holes and electrons. This observation can be attributed to the position of electron affinity and ionization potential of these systems in the trap-free window.[53] The presented approach thus provides a route to comprehensively assess the performance of non-fullerene acceptors and aids in comprehending the underlying electronic processes governing the photophysics of these novel molecules.

SUPPLEMENTARY MATERIAL

The supplementary material contains the chemical structure, electrostatic potential surfaces, frontier molecular orbitals, MD simulated morphology, and tables of photovoltaic parameters and computed quantities.

ACKNOWLEDGMENTS

AUTHOR DECLARATIONS

Conflict of Interest

The authors have no conflicts to disclose.

Author Contributions

K.P. and R.K. contributed equally to this work.

Khantil Patel: Data curation (equal); Formal analysis (equal); Investigation (equal); Methodology (equal); Validation (equal); Writing – original draft (equal). **Rudranarayan Khatua**: Data curation (equal); Formal analysis (equal); Investigation (equal); Methodology (equal); Validation (equal); Writing – original draft (equal); Writing – review & editing (equal). **Kalyani Patrikar**: Data curation (supporting); Formal analysis (supporting); Investigation (supporting); Methodology (supporting); Validation (equal); Writing – review & editing (equal). **Anirban Mondal**: Conceptualization (lead); Formal analysis (equal); Funding acquisition (lead); Investigation (equal); Methodology (equal); Project administration (lead); Resources (lead); Supervision (lead); Validation (equal); Writing – original draft (lead); Writing – review & editing (lead).

DATA AVAILABILITY

The data that support the findings of this study are available from the corresponding author upon reasonable request.

REFERENCES

[1] J. Hou, O. Inganäs, R. H. Friend, and F. Gao, "Organic solar cells based on non-fullerene acceptors," Nat. Mater. **17**, 119–128 (2018).

[2] C. Yan, S. Barlow, Z. Wang, H. Yan, A. K.-Y. Jen, S. R. Marder, and X. Zhan, "Non-fullerene acceptors for organic solar cells," Nat. Rev. Mater. **3**, 18003 (2018).

[3] Z. Zhang, J. Yuan, Q. Wei, and Y. Zou, "Small-molecule electron acceptors for efficient non-fullerene organic solar cells," Front. Chem. **6**, 414 (2018).

[4] J. Zhang, H. S. Tan, X. Guo, A. Facchetti, and H. Yan, "Material insights and challenges for non-fullerene organic solar cells based on small molecular acceptors," Nat. Energy **3**, 720–731 (2018).

[5] D. Zhou, J. Wang, Z. Xu, H. Xu, J. Quan, J. Deng, Y. Li, Y. Tong, B. Hu, and L. Chen, "Recent advances of nonfullerene acceptors in organic solar cells," Nano Energy **103**, 107802 (2022).

[6] K. Liu, Y. Jiang, F. Liu, G. Ran, F. Huang, W. Wang, W. Zhang, C. Zhang, J. Hou, and X. Zhu, "Organic solar cells with over 19% efficiency enabled by a 2D-conjugated non-fullerene acceptor featuring favorable electronic and aggregation structures," Adv. Mater. **35**, 2300363 (2023).

[7] H. Chen, S. Y. Jeong, J. Tian, Y. Zhang, D. R. Naphade, M. Alsufyani, W. Zhang, S. Griggs, H. Hu, S. Barlow *et al.*, "A 19% efficient and stable organic photovoltaic device enabled by a guest nonfullerene acceptor with fibril-like morphology," Energy Environ. Sci. **16**, 1062–1070 (2023).

[8] Y. He, S. Alem, J. Lu, N. Yee, and Y. Tao, "A new non-fullerene acceptor based on an asymmetric electron-deficient core for indoor organic photovoltaic cells," Mater. Chem. Phys. **306**, 128036 (2023).

[9] Z. Luo, T. Xu, C. Zhang, and C. Yang, "Side-chain engineering of non-fullerene small-molecule acceptors for organic solar cells," Energy Environ. Sci. **16**, 2732–2758 (2023).

[10] S. Suman and S. P. Singh, "Impact of end groups on the performance of non-fullerene acceptors for organic solar cell applications," J. Mater. Chem. A **7**, 22701–22729 (2019).

[11] R. Khatua, B. Das, and A. Mondal, "Rational design of non-fullerene acceptors via side-chain and terminal group engineering: A computational study," Phys. Chem. Chem. Phys. **25**, 7994–8004 (2023).

[12] Y. Wang, Y. Wang, B. Kan, X. Ke, X. Wan, C. Li, and Y. Chen, "High-performance all-small-molecule solar cells based on a new type of small molecule acceptors with chlorinated end groups," Adv. Energy Mater. **8**, 1802021 (2018).

[13] R. Geng, X. Song, H. Feng, J. Yu, M. Zhang, N. Gasparini, Z. Zhang, F. Liu, D. Baran, and W. Tang, "Nonfullerene acceptor for organic solar cells with chlorination on dithieno[3,2-*b*:2′,3′-*d*]pyrrol fused-ring," ACS Energy Lett. **4**, 763–770 (2019).

[14] S. Lu, F. Li, K. Zhang, J. Zhu, W. Cui, R. Yang, L. Yu, and M. Sun, "Halogenation on terminal groups of ITIC based electron acceptors as an effective strategy for efficient polymer solar cells," Sol. Energy **195**, 429–435 (2020).

[15] G. Kupgan, X.-K. Chen, and J.-L. Bredas, "Molecular packing of non-fullerene acceptors for organic solar cells: Distinctive local morphology in Y6 vs. ITIC derivatives," Mater. Today Adv. **11**, 100154 (2021).

[16] C. He, Y. Li, S. Li, Z.-P. Yu, Y. Li, X. Lu, M. Shi, C.-Z. Li, and H. Chen, "Near-infrared electron acceptors with unfused architecture for efficient organic solar cells," ACS Appl. Mater. Interfaces **12**, 16700–16706 (2020).

[17] S. Li, L. Zhan, T.-K. Lau, Z.-P. Yu, W. Yang, T. R. Andersen, Z. Fu, C.-Z. Li, X. Lu, M. Shi, and H. Chen, "Near-Infrared nonfullerene acceptors based on benzobis(thiazole) unit for efficient organic solar cells with low energy loss," Small Methods **3**, 1900531 (2019).

[18] X. Liu, Y. Wei, X. Zhang, L. Qin, Z. Wei, and H. Huang, "An A-D-A′-D-A type unfused nonfullerene acceptor for organic solar cells with approaching 14% efficiency," Sci. China Chem. **64**, 228–231 (2021).

[19] Z. Jia, Q. Ma, Z. Chen, L. Meng, N. Jain, I. Angunawela, S. Qin, X. Kong, X. Li, Y. Yang *et al.*, "Near-infrared absorbing acceptor with suppressed triplet exciton generation enabling high performance tandem organic solar cells," Nat. Commun. **14**, 1236 (2023).

[20] A. Markina, K.-H. Lin, W. Liu, C. Poelking, Y. Firdaus, D. R. Villalva, J. I. Khan, S. H. Paleti, G. T. Harrison, J. Gorenflot *et al.*, "Chemical design rules for non-fullerene acceptors in organic solar cells," Adv. Energy Mater. **11**, 2102363 (2021).

[21] S. M. Swick, W. Zhu, M. Matta, T. J. Aldrich, A. Harbuzaru, J. T. Lopez Navarrete, R. Ponce Ortiz, K. L. Kohlstedt, G. C. Schatz, A. Facchetti et al., "Closely packed, low reorganization energy π-extended postfullerene acceptors for efficient polymer solar cells," Proc. Natl. Acad. Sci. U. S. A. **115**, E8341–E8348 (2018).

[22] S. A. Lopez, B. Sanchez-Lengeling, J. de Goes Soares, and A. Aspuru-Guzik, "Design principles and top non-fullerene acceptor candidates for organic photovoltaics," Joule **1**, 857–870 (2017).

[23] T. Wang and J.-L. Brédas, "Organic solar cells based on non-fullerene small-molecule acceptors: Impact of substituent position," Matter **2**, 119–135 (2020).

[24] T. Wang and J.-L. Brédas, "Nonfullerene small-molecule acceptors for organic photovoltaics: Understanding the impact of methoxy substitution position on molecular packing and electron-transfer properties," Adv. Funct. Mater. **29**, 1806845 (2019).

[25] T. Korzdorfer and J.-L. Bredas, "Organic electronic materials: Recent advances in the DFT description of the ground and excited states using tuned range-separated hybrid functionals," Acc. Chem. Res. **47**, 3284–3291 (2014).

[26] H. Yu, Z. Qi, X. Li, Z. Wang, W. Zhou, H. Ade, H. Yan, and K. Chen, "Modulating energy level on an A-D-A′-D-A-type unfused acceptor by a benzothiadiazole core enables organic solar cells with simple procedure and high performance," Sol. RRL **4**, 2000421 (2020).

[27] M. J. Frisch, G. W. Trucks, H. B. Schlegel, G. E. Scuseria, M. A. Robb, J. R. Cheeseman, G. Scalmani, V. Barone, B. Mennucci, G. A. Petersson, H. Nakatsuji, M. Caricato, X. Li, H. P. Hratchian, A. F. Izmaylov, J. Bloino, G. Zheng, J. L. Sonnenberg, M. Hada, M. Ehara, K. Toyota, R. Fukuda, J. Hasegawa, M. Ishida, T. Nakajima, Y. Honda, O. Kitao, H. Nakai, T. Vreven, J. A. Montgomery, Jr., J. E. Peralta, F. Ogliaro, M. Bearpark, J. J. Heyd, E. Brothers, K. N. Kudin, V. N. Staroverov, R. Kobayashi, J. Normand, K. Raghavachari, A. Rendell, J. C. Burant, S. S. Iyengar, J. Tomasi, M. Cossi, N. Rega, J. M. Millam, M. Klene, J. E. Knox, J. B. Cross, V. Bakken, C. Adamo, J. Jaramillo, R. Gomperts, R. E. Stratmann, O. Yazyev, A. J. Austin, R. Cammi, C. Pomelli, J. W. Ochterski, R. L. Martin, K. Morokuma, V. G. Zakrzewski, G. A. Voth, P. Salvador, J. J. Dannenberg, S. Dapprich, A. D. Daniels, Ö. Farkas, J. B. Foresman, J. V. Ortiz, J. Cioslowski, and D. J. Fox, *Gaussian 09, Revision E.01*, Gaussian, Inc., Wallingford, CT, 2009.

[28] E. Runge and E. K. Gross, "Density-functional theory for time-dependent systems," Phys. Rev. Lett. **52**, 997 (1984).

[29] V. Barone and M. Cossi, "Quantum calculation of molecular energies and energy gradients in solution by a conductor solvent model," J. Phys. Chem. A **102**, 1995–2001 (1998).

[30] S. Refaely-Abramson, R. Baer, and L. Kronik, "Fundamental and excitation gaps in molecules of relevance for organic photovoltaics from an optimally tuned range-separated hybrid functional," Phys. Rev. B **84**, 075144 (2011).

[31] O. S. Bokareva, G. Grell, S. I. Bokarev, and O. Kuhn, "Tuning range-separated density functional theory for photocatalytic water splitting systems," J. Chem. Theory Comput. **11**, 1700–1709 (2015).

[32] M. Cossi, V. Barone, R. Cammi, and J. Tomasi, "Ab initio study of solvated molecules: A new implementation of the polarizable continuum model," Chem. Phys. Lett. **255**, 327–335 (1996).

[33] B. Mennucci, "Polarizable continuum model," Wiley Interdiscip. Rev.: Comput. Mol. Sci. **2**, 386–404 (2012).

[34] R. Khatua and A. Mondal, "Design and screening of B–N functionalized non-fullerene acceptors for organic solar cells via multiscale computation," Mater. Adv. **4**, 4425–4435 (2023).

[35] M.-H. Lee, "Identifying correlation between the open-circuit voltage and the Frontier orbital energies of non-fullerene organic solar cells based on interpretable machine-learning approaches," Sol. Energy **234**, 360–367 (2022).

[36] A. J. Stone, "Distributed multipole analysis: Stability for large basis sets," J. Chem. Theory Comput. **1**, 1128–1132 (2005).

[37] B. Hess, C. Kutzner, D. Van Der Spoel, and E. Lindahl, "GROMACS 4: Algorithms for highly efficient, load-balanced, and scalable molecular simulation," J. Chem. Theory Comput. **4**, 435–447 (2008).

[38] S. Pronk, S. Páll, R. Schulz, P. Larsson, P. Bjelkmar, R. Apostolov, M. R. Shirts, J. C. Smith, P. M. Kasson, D. van der Spoel, B. Hess, and E. Lindahl, "GROMACS 4.5: A high-throughput and highly parallel open source molecular simulation toolkit," Bioinformatics **29**, 845–854 (2013).

[39] W. L. Jorgensen, D. S. Maxwell, and J. Tirado-Rives, "Development and testing of the OPLS all-atom force field on conformational energetics and properties of organic liquids," J. Am. Chem. Soc. **118**, 11225–11236 (1996).

[40] W. L. Jorgensen and J. Tirado-Rives, "Potential energy functions for atomic-level simulations of water and organic and biomolecular systems," Proc. Natl. Acad. Sci. U. S. A. **102**, 6665–6670 (2005).

[41] D. J. Cole, J. Z. Vilseck, J. Tirado-Rives, M. C. Payne, and W. L. Jorgensen, "Biomolecular force field parameterization via atoms-in-molecule electron density partitioning," J. Chem. Theory Comput. **12**, 2312–2323 (2016).

[42] T. A. Manz and N. G. Limas, "Introducing DDEC6 atomic population analysis: Part 1. Charge partitioning theory and methodology," RSC Adv. **6**, 47771–47801 (2016).

[43] A. Tkatchenko and M. Scheffler, "Accurate molecular van der Waals interactions from ground-state electron density and free-atom reference data," Phys. Rev. Lett. **102**, 073005 (2009).

[44] L. Martínez, R. Andrade, E. G. Birgin, and J. M. Martínez, "PACKMOL: A package for building initial configurations for molecular dynamics simulations," J. Comput. Chem. **30**, 2157–2164 (2009).

[45] G. Bussi, D. Donadio, and M. Parrinello, "Canonical sampling through velocity rescaling," J. Chem. Phys. **126**, 014101 (2007).

[46] H. J. C. Berendsen, J. P. M. Postma, W. F. van Gunsteren, A. DiNola, and J. R. Haak, "Molecular dynamics with coupling to an external bath," J. Chem. Phys. **81**, 3684–3690 (1984).

[47] J. Brown (2023). "Brown's open access toolset BOAT," GitHub. https://joshuasbrown.github.io/docs/CATNIP/catnip_home.html

[48] R. A. Marcus, "On the theory of oxidation-reduction reactions involving electron transfer. I," J. Chem. Phys. **24**, 966–978 (1956).

[49] E. F. Valeev, V. Coropceanu, D. A. da Silva Filho, S. Salman, and J.-L. Brédas, "Effect of electronic polarization on charge-transport parameters in molecular organic semiconductors," J. Am. Chem. Soc. **128**, 9882–9886 (2006).

[50] R. P. Fornari, J. Aragó, and A. Troisi, "A very general rate expression for charge hopping in semiconducting polymers," J. Chem. Phys. **142**, 184105 (2015).

[51] G. Bary, L. Ghani, M. I. Jamil, M. Arslan, W. Ahmed, A. Ahmad, M. Sajid, R. Ahmad, and D. Huang, "Designing small organic non-fullerene acceptor molecules with diflorobenzene or quinoline core and dithiophene donor moiety through density functional theory," Sci. Rep. **11**, 19683 (2021).

[52] J. Wang, Y. Cui, Z. Chen, J. Zhang, Y. Xiao, T. Zhang, W. Wang, Y. Xu, N. Yang, H. Yao et al., "A wide bandgap acceptor with large dielectric constant and high electrostatic potential values for efficient organic photovoltaic cells," J. Am. Chem. Soc. **145**, 13686–13695 (2023).

[53] N. B. Kotadiya, A. Mondal, P. W. M. Blom, D. Andrienko, and G.-J. A. H. Wetzelaer, "A window to trap-free charge transport in organic semiconducting thin films," Nat. Mater. **18**, 1182–1186 (2019).

[54] S. Karuthedath, J. Gorenflot, Y. Firdaus, N. Chaturvedi, C. S. De Castro, G. T. Harrison, J. I. Khan, A. Markina, A. H. Balawi, T. A. D. Pena et al., "Intrinsic efficiency limits in low-bandgap non-fullerene acceptor organic solar cells," Nat. Mater. **20**, 378–384 (2021).

[55] A. Kuzmich, D. Padula, H. Ma, and A. Troisi, "Trends in the electronic and geometric structure of non-fullerene based acceptors for organic solar cells," Energy Environ. Sci. **10**, 395–401 (2017).

[56] T. Liu and A. Troisi, "Absolute rate of charge separation and recombination in a molecular model of the P3HT/PCBM interface," J. Phys. Chem. C **115**, 2406–2415 (2011).

[57] M. Andrea, K. Kordos, E. Lidorikis, and D. Papageorgiou, "Molecular description of charge transport in the IDIC non-fullerene acceptor for organic solar cells," Comput. Mater. Sci. **202**, 110978 (2022).